Journal of
Marine Science and Engineering

MDPI

Article

Computational Study of Overtopping Phenomenon over Cylindrical Structures Including Mitigation Structures

Gustavo A. Esteban *, Xabier Ezkurra, Iñigo Bidaguren, Iñigo Albaina and Urko Izquierdo

Energy Engineering Department, Universidad del País Vasco/Euskal Herriko Unibertsitatea (UPV/EHU), Pza. Ingeniero Torres Quevedo 1, E-48013 Bilbao, Spain; xezkurra002@ikasle.ehu.eus (X.E.); i.bidaguren@ehu.eus (I.B.); i.albaina@ehu.eus (I.A.); urko.izquierdo@ehu.eus (U.I.)

* Correspondence: gustavo.esteban@ehu.eus

Abstract: Wave overtopping occurring in offshore wind renewable energy structures such as tension leg platforms (TLPs) or semi-submersible platforms is a phenomenon that is worth studying and preventing in order to extend the remaining useful life of the corresponding facilities. The behaviour of this phenomenon has been extensively reported for linear coastal defences like seawalls. However, no referenced study has treated the case of cylindrical structures typical of these applications to a similar extent. The aim of the present study is to define an empirical expression that portrays the relative overtopping rate over a vertical cylinder including a variety of bull-nose type mitigation structures to reduce the overtopping rate in the same fashion as for the linear structures characteristic of shoreline defences. Hydrodynamic interaction was studied by means of an experimentally validated numerical model applied to a non-impulsive regular wave regime and the results were compared with the case of a plain cylinder to evaluate the expected improvement in the overtopping performance. Four different types of parapets were added to the crest of the base cylinder, with different parapet height and horizontal extension, to see the influence of the geometry on the mitigation efficiency. Computational results confirmed the effectivity of the proposed solution in the overtopping reduction, though the singularity of each parapet geometry did not lead to an outstanding difference between the analysed options. Consequently, the resulting overtopping decrease in all the proposed geometries could be modelled by a unique specific Weibull-type function of the relative freeboard, which governed the phenomenon, showing a net reduction in comparison with the cylinder without the geometric modifications. In addition, the relationship between the reduced relative overtopping rate and the mean flow thickness over the vertical cylinder crest was studied as an alternative methodology to assess the potential damage caused by overtopping in real structures without complex volumetric measurements. The collection of computational results was fitted to a useful function, allowing for the definition of the overtopping discharge once the mean flow thickness was known.

Keywords: wave overtopping; overtopping discharge; cylindrical structure; numerical wave flume; bull-nose; parapet; wave return wall

Citation: Esteban, G.A.; Ezkurra, X.; Bidaguren, I.; Albaina, I.; Izquierdo, U. Computational Study of Overtopping Phenomenon over Cylindrical Structures Including Mitigation Structures. *J. Mar. Sci. Eng.* **2024**, *12*, 1441. https://doi.org/10.3390/jmse12081441

Academic Editor: Claudio Lugni

Received: 11 July 2024
Revised: 1 August 2024
Accepted: 15 August 2024
Published: 20 August 2024

1. Introduction

Overtopping is a nonlinear phenomenon that occurs when a wave or a fraction of a wave surpasses a fixed or floating structure and generates a layer of water over its crest that can cause flooding or surface damage. It is a well-established phenomenon, and it is considered in the design phase of fixed and floating structures in the marine energy sector because it can damage the structures or facilities mounted on top, other than modifying the expected oscillation response to the incident wave train affecting the operation of the wind turbine [1–3]. The standard measures taken against overtopping are developed for defence structures like breakwaters, dikes or seawalls, which are implemented in marine structures exposed to waves such as shoreline promenades, ports or harbours.

In order to develop effective designs of protective structures, there has been a continuous effort to study, understand and characterise overtopping. The study of overtopping was carried out independently by different research groups during its first stages, but the development of the CLASH project introduced a common database and a standardised methodology to study overtopping [4]. After the completion of the project, the *EurOtop* manual [5] was published in 2007, gathering all the information from different databases in a single collection and proposing the corresponding representative unified analytical predictive models. The *EurOtop* manual became the main reference for overtopping, and a second edition was published in 2018 [6] with new findings and improvements.

The methodology employed by most groups that study overtopping is to measure the overtopping discharge over a scaled physical model tested in an experimental wave flume or a numerical wave flume (NMF) by using computational fluid dynamics (CFD) calculations. The elements required for both the experimental and the numerical procedures are a wavemaker system, a wave height measuring system and a procedure to measure the overtopped water volume.

On the one hand, the experimental procedure implies wave generation by a pulsating paddle with piston-type linear motion and/or a reciprocating oscillation of a flap around a hinge. The generated wave at one end of the flume develops and propagates towards the specific structure under study and the opposite end of the flume where wave reflection may occur [7]. To minimise the effect of reflection, passive and active absorption systems are normally used. Sometimes the effective time intervals of the tests are limited to the periods where a reflected wave travels backwards to the generation system and back again to the testing area after re-reflection on the wavemaker [8]. There are different systems to measure the generated waves by monitoring the free surface position to infer the incident wave height, period and wavelength. With regard to overtopping characterisation, a calibrated tank is placed at the end of the main structure to measure and accumulate the overtopped liquid volume or mass. As an example, representative recent experimental tests in flumes measure the overtopping discharge over specific structures occurring in the case of tsunami-types waves generated in the sea or onshore from glacier calving [9–11].

On the other hand, in the case of the computational approach, the simulations are performed by numerically solving the conservation laws of fluid motion that can be expressed in either the Eulerian or the Lagrangian approach. The Eulerian approach discretises the working volume into a fine mesh formed by cells containing nodes where the solutions of the equations are numerically calculated following the finite volume method. On the other hand, the Lagrangian approach manages fluid particles or blobs, to which fluid equations are applied, with models such as smoothed particle hydrodynamics (SPH) [12]. Different representative late examples of the application of the Eulerian approach based on the volume of fluid (VOF) method [13] (based on Reynolds-averaged Navier–Stokes (RANS)) have succeeded in describing and evaluating the overtopping discharge over structures to study the influence of the associated hydraulic load and erosion, geometry design influence, damaged/upgraded state of breakwaters and corresponding modification of the overtopped layer thickness and its velocity [14–18]. Moreover, the SPH method has been proven to be a successful alternative for studying overtopping on different seawalls, decks and dams [19,20].

The different structure options and the corresponding parameters to mitigate the overtopping phenomenon are reported in [5]. In search of overtopping prediction by representative models, van de Meer et al. [21] proposed to use a reunified Weibull-type function valid for the whole range from zero freeboard conditions, different wave breaking/non-breaking conditions, diverse nature of the foreshore, composite structures and variation of the slope. The last updates on the issue were incorporated in the second edition of the *EurOtop* manual [6]. Special mention should be made to Zanuttigh and Formentin for their renowned study about extreme and admissible overtopping discharges using a special neural network [22] and the impact of crown walls with parapets [23,24]. Some other research works regarding overtopping address the forces acting on the defence structures due to

wave impacts, which are studied to ensure the physical integrity of the structure; research by Van Doorslaer and De Rouck [25,26] and those by Martinelli and Castellino et al. [27–29] are worth highlighting in relation to the evaluation of wave return walls.

With regard to the different solutions applied to reduce overtopping discharge under extreme sea states, it is common practice to modify the foreshore by introducing breakwaters, slopes, promenades or wave run-ups [18,30–32]. These solutions are specifically designed to prevent inland flooding, and are out of the applicability to the vertical structures installed in offshore floating systems. For that reason, this study focuses on common geometric modifications of the main structure facing the wave front, like chamfers, recurved walls or parapets [33–39]. More specifically, among all these types of geometry, parapets have been chosen in this study because they represent the main option applied to vertical walls and they are reported to work properly. In this case, the reduction of overtopping is based on the flow deflection provoked by the parapet that sends back the up-rushing water volume in the direction of the wave that is coming in.

The procedure followed in this campaign is based on numerical simulations of the overtopping discharge over a fixed vertical cylinder with parapet rings mounted on top, for comparison with results obtained in previous research [40], where the overtopping discharge was defined for a plain cylinder in the same wave conditions and base geometry (i.e., diameter or free-board range). The computational configuration in the CFD model used here follows the same RANS-VOF arrangement as the one already validated with the corresponding experimental campaign [40]. This way, the expected overtopping rate reduction is evaluated to analyse whether the proposed structural modifications are a viable alternative to prevent over dimensioning the main cylindrical structures in real facilities in search of overtopping performance of the final structure configuration.

An additional secondary aspect treated here is the study of the relation between the relative overtopping discharge and nondimensionalised mean flow thickness of the water sheet flowing over the structure. This approach would offer a practical methodology to assess overtopping discharges by a simple measurement of water elevation on the crest of the platform instead of mounting complex water collection structures to measure the overtopped volume. The instantaneous height of the flow thickness could be measured with a wave probe in a simpler and cost-effective way.

This study is the basic step and fundamental basis before tackling the problem of overtopping subjected to floating structures typical of offshore energy technologies with these cylinder-based geometric characteristics like TLP or semi-submersible platforms.

2. Theoretical Background

The total overtopping discharge over a structure may contain three different wave overtopping contributions: green water overtopping, white water overtopping and overtopping due to spray. Green water overtopping is characterised by the non-impulsive regime where the wave height is enough for the wave to form a continuous layer over the structure. Contrarily, white water overtopping occurs in the impulsive regime when waves break against the area of the structure facing the incoming wave front, producing large masses of water mixed with entrained air that move over the structure because of the momentum and inertia of the water moving mass. Spray overtopping accounts for the interaction between wave crests and wind, its contribution being considered negligible in normal engineering contexts.

Wave overtopping is affected by a multitude of properties that contain both the characteristics of the sea state and the structure's geometry and foreshore. The primary factors considered in the analysis of sea state effects on overtopping include wave period (T), wave height (H), water depth (h) and wave steepness (s) at the base of the structure. Additionally, geometric attributes of the structure are considered, such as the berm, the foreshore slope and, specially, the crest freeboard (R_c), which is associated with the height of the structure (H_c). The crest freeboard is known to be a critical parameter in the study of wave overtopping. In the case of the use of parapets as overtopping mitigation structures,

additional key parameters influencing the phenomenon are the parapet height (h_r) and the horizontal extension of the parapet (B_r) (Figure 1).

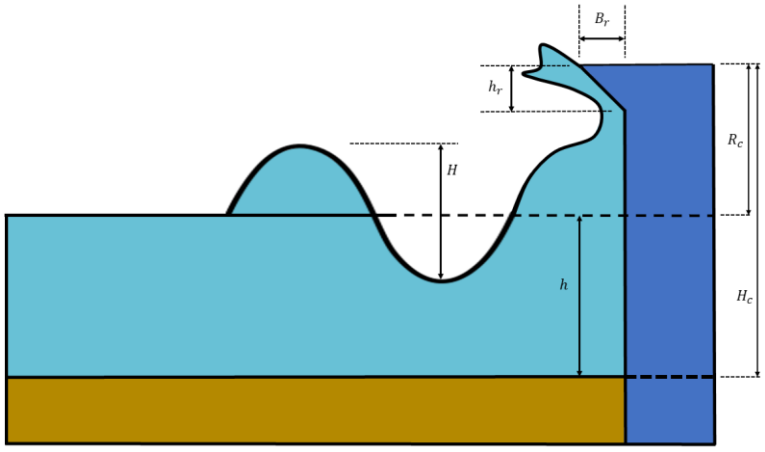

Figure 1. Main parameters that affect the overtopping phenomenon in a vertical wall including a parapet. (Original elaboration based on Figure 7.21 of *EurOtop* manual [6]).

Describing wave overtopping is challenging because of its nonlinear nature and, thus, it is not well represented by simple analytical models. The evaluation of wave overtopping for a specific structure typically involves the utilisation of empirical expressions derived from CFD simulations or experiments with scaled physical models. Both methods are particularly valuable in assessing wave overtopping, as this phenomenon is influenced by a variety of factors with interconnected impacts that are difficult to predict. The empirical approach contains a simple representation of the underlying physics of the phenomenon, often presented as an equation that correlates dimensionless parameters specific to the process (e.g., overtopping discharge, wave attributes and structural geometric factors).

The main objective parameter in this analysis is the mean overtopping flow discharge q (m^2/s), which accounts for the average liquid volume per unit time and transversal horizontal length of structure passing over, which is usually presented in its nondimensional form (by dividing by $\sqrt{g{H_{m0}}^3}$), known as the relative overtopping rate. The significant wave height (H_{m0}) equals four times the root mean square displacement of the free surface, which is equivalent to the average height of the 1/3 highest waves of a series of irregular waves, and g is the acceleration of gravity.

The dependence of the relative overtopping rate is normally defined as a function of the crest freeboard R_c, being the elevation difference between the structure crest and the still water level (SWL), which is given, again, in a nondimensionalised form (by dividing by the significant wave height H_{m0}) known as the relative freeboard.

To assess the wave overtopping accurately, it is necessary to identify the wave–structure interaction regime because different processes and outcomes may occur in different scenarios. Specifically, when dealing with vertical walls with structural modifications, overtopping can occur under two distinct regimes: non-impulsive and impulsive conditions. Non-impulsive conditions happen when wave heights are relatively modest compared with the depth at the base of the structure, and the wave steepness remains low, staying far from the point of breaking. In such a situation, overtopping waves generate smoothly evolving loads, and water flows gently over the structure. In contrast, impulsive conditions happen at vertical or steep walls when wave heights significantly exceed local water depths and show a high wave steepness. In this scenario, the waves crash against the structure, giving rise to a fast, vertical and jet-like flow of water that jumps over the structure due to

momentum and inertia. The likelihood of having impulsive or non-impulsive overtopping is discriminated by employing the "impulsiveness" constant defined in Equation (1) [6]:

$$h^* = \frac{h^2}{H_{m0} L_{m-1,0}} \tag{1}$$

where $L_{m-1,0} = g(T_{m-1,0})^2/2\pi$ is the deep-water wavelength corresponding to the wave energy period $T_{m-1,0}$. From $h^* > 0.23$ onwards, waves are considered non-impulsive.

Another effect that may have a decisive influence is the existence of a sloping foreshore at a shallow or intermediate depth because it may cause shoaling and/or breaking during its propagation towards the structure susceptible to overtopping. All these different responses corresponding to different regimes are summarised in Figure 2.

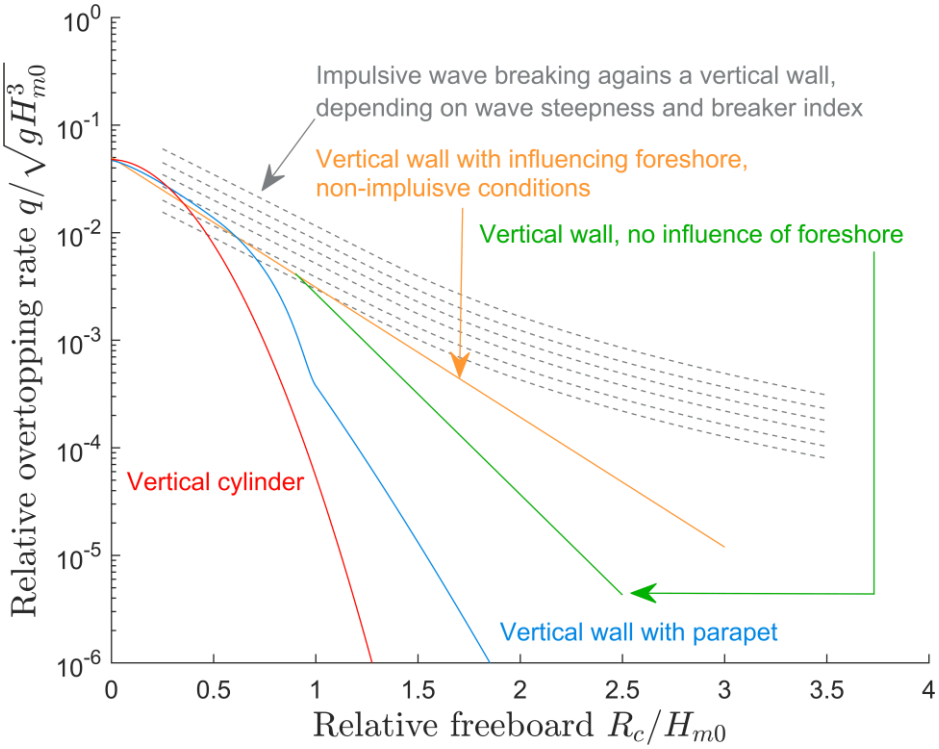

Figure 2. Overview of different overtopping regimes on vertical walls and cylinders [6,21,40–42].

In addition, it is noticeable in Figure 2, on the one hand, the difference between the relative overtopping discharge produced over a linear vertical wall (green line) and the one produced over a cylindrical structure (red line) and, on the other hand, the reduction introduced by a parapet (blue line) with respect to the reference vertical wall (green line). The objective here is to account for the overtopping reduction expected for a cylindrical structured with similar parapets mounted below the crown of the cylinder under the same non-impulsive wave regime.

The widespread empirical model for predicting wave overtopping takes the form of a Weibull function (2) proposed by van der Meer et al. [6]:

$$\frac{q}{\sqrt{g{H_{m0}}^3}} = a \cdot \exp\left[-\left(b\frac{R_c}{H_{m0}}\right)^c\right] \tag{2}$$

Parameter R_c/H_{m0}, known as the relative freeboard, is the governing parameter of Equation (2), together with the significant wave height. Equation (2) is the nondimensionalised expression covering the whole range of the relative freeboard. Parameters a, b and c depend on the case study, including the different wave regimes mentioned before, and are determined

from empirical results obtained either experimentally or numerically. This is an important equation when evaluating whether tolerable overtopping limit is surpassed or not under a certain harsh sea state. Even if only the tolerable limits are well defined for coast defences in [6] (for example, a larger yacht in a port with some facilities installed on deck has a limit of $q < 5$ L/s per m for $H_{m0} > 5$ m), as it is not yet publicly established for floating offshore wind turbines, this design criterion will be of high relevance towards the implementation of the technology to make it commercially competitive.

In the case of studying regular waves, the resulting overtopping discharge is known to overestimate the results obtained with the Rayleigh distribution, characterised by the corresponding significant wave height; a factor between 2.3 and 2.8 is reported in [43]. Consequently, the results obtained with regular waves can be taken as conservative values of the corresponding ones obtained with the spectra characterised by the same significant wave heights in such a comparison.

The reference equations to predict overtopping with no influence of the foreshore and under non-impulsive regular waves for a vertical wall [6] (3) and a vertical cylinder without any parapet [40] (4) are as follows:

$$\frac{q}{\sqrt{g{H_{m0}}^3}} = 0.047 \cdot \exp\left[-\left(2.35\frac{R_c}{H}\right)^{1.3}\right] \tag{3}$$

$$\frac{Q}{\sqrt{gH^3D}} = 0.0478 \cdot \exp\left[-\left(2.74\frac{R_c}{H}\right)^{1.9}\right] \tag{4}$$

The introduction of a parapet to the geometry is expected to result in a drop in the overtopping flow discharge over the structure, and to correspondingly modify the previous expressions. However, the effectiveness of the mitigation structure is highly related to the value of the relative freeboard. Within a low relative freeboard regime ($R_c/H \leq 0.5$), the parapet becomes easily submerged under the overtopped water flow, whereas, in a high relative freeboard regime ($R_c/H > 1.0$), there is a maximum performance of the parapet because of the resulting effective seaward projection of the incoming wave. Between these two differentiated regimes, there is an intermediate regime ($1.0 \geq R_c/H > 0.5$) with a medium efficiency in the overtopping reduction.

Consequently, the best way to account for the reduction due to the introduction of a parapet is defined in the *EurOtop* manual [6] as a piecewise regression (Figure 2). This same approach has been followed for the cylindrical case accounting for the intermediate and low relative freeboard range covered in this piece of research with the following fitting function:

$$\frac{Q}{\sqrt{gH^3D}} = \begin{Bmatrix} a \cdot \exp\left[-\left(b\frac{R_c}{H}\right)^c\right], & \frac{R_c}{H} \leq 0.5 \\ d \cdot \exp\left[-\left(e\frac{R_c}{H}\right)^f\right], & \frac{R_c}{H} > 0.5 \end{Bmatrix} \tag{5}$$

Other than the overtopping flow rate, the overtopping flow thickness δ is also studied in this campaign. This parameter defines the thickness of the liquid layer passing over the main structure during an overtopping event. In the particular case of the cylinder, it is evaluated at the centre of the crest (the axis of the cylinder). The average flow thickness $\overline{\delta}$ is computed by averaging the instantaneous signal of the variable over the time interval taken by the interaction under study Δt:

$$\overline{\delta} = \frac{1}{\Delta t}\int_0^{\Delta t} \delta(t)dt \tag{6}$$

This parameter will be computed, and its relationship with the overtopping discharge addressed in Section 4.

3. Aims and Methods

The objective of the present study is to determine the relationship between the geometric characteristics of the cylinder with the selected options of parapet and wave overtopping discharge. As a result, a model based on predictive equations for fixed vertical cylinder with parapets will be proposed.

In this campaign, a numerical model that was used and experimentally validated in a previous campaign [40] was used for the analysis. That research study conducted a numerical calculation of wave overtopping on a fixed vertical cylinder affected by regular waves, and the corresponding experimental analysis for its validation. In the current study, the experimentally validated numerical model was used to analyse the consequence of the specific geometry modification of the parapet mounted on the top part of the cylinder.

3.1. Test Programme

All the simulations were executed with regular waves, considering wave heights from H = 0.065 m to 0.160 m and period T = 1.3 s. The period was not varied because its influence has been reported to be negligible on the dimensionless representation of the overtopping discharge [40]. In fact, no dependence on the period or wavelength was stated in the empirical models represented in Figure 2 and the corresponding well-established Equations (2)–(4). The values were determined through the application of Froude similitude with a reduction scale factor of 1:100 corresponding to wave heights of 6.5 m to 16 m and a period of 13 s of extreme sea state. These wave conditions are typical of Beaufort numbers in the range 9–11, which correspond to a violent storm. A constant water depth of h = 0.32 m for the model was maintained in all the experiments.

The cylinder showed a diameter of D = 0.11 m, which was 11 m in full scale. Four different cylinder heights were simulated, covering a range of freeboard R_c from 0.02 to 0.07 m in the empirical model (Table 1), by taking into account the design parameters of the ballast cylindrical columns of the NATULUS-10 floating offshore wind turbine [44]. The wave height H was varied within the aforementioned range for each individual freeboard case in order to manage a uniformly distributed range of relative freeboard R_c/H values with overlapping transition frames between cases. A broad range was studied for the relative freeboard between 0.14 and 0.78, amounting to 24 values (6 values of wave height for each freeboard case).

Table 1. Wave sets used in this campaign.

	R_c (m)	R_c/H
Case 1	0.020	0.143, 0.167, 0.200, 0.222, 0.267, 0.308
Case 2	0.037	0.229, 0.282, 0.319, 0.367, 0.431, 0.489
Case 3	0.053	0.333, 0.381, 0.427, 0.458, 0.533, 0.593
Case 4	0.070	0.500, 0.538, 0.583, 0.636, 0.700, 0.778

It is customary in the study of parapets to define the height of the parapet h_r as a function of the crest freeboard R_c, and the horizontal extension of the parapet B_r as a function of the height of the parapet h_r [24,33]. The studies used as references for geometric ratios in parapets in search of better overtopping performance [34] recommend beginning the study of parapets in the range of $h_r/B_r \in [0.5, 1]$. Therefore, the four geometries studied here were chosen to study both limit ratios with two different parapet heights (Table 2 and Figure 3).

Table 2. Geometries studied in this campaign.

	h_r (m)	B_r (m)
Geometry 1	0.021	0.021
Geometry 2	0.021	0.042
Geometry 3	0.028	0.028
Geometry 4	0.028	0.056

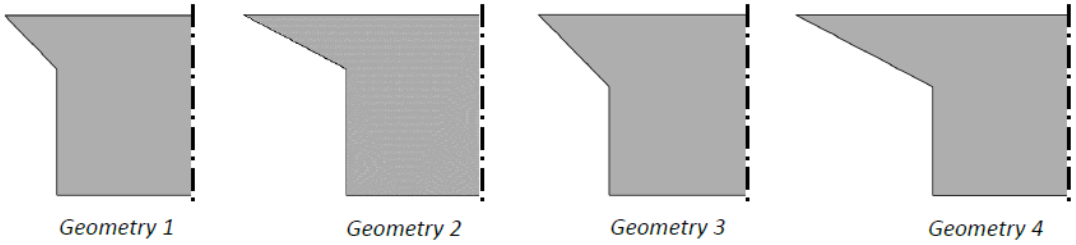

Figure 3. Visualisation of parapet geometries. The total height represented is the maximum crest freeboard. The axial-symmetric cross-section is represented.

Each of the four parapet geometries was exposed to the same wave campaign, amounting to a total of 96 computational cases. The range of "impulsiveness" considered during the experiments started at 0.243 and went up to 0.466, all of them greater than the limit value of 0.23 and consequently belonging to the non-impulsive regime. "Impulsiveness" and breaking waves were closely related. And, because the objective was to characterise the non-impulsive regime, the test campaign covered the non-breaking regime. In this case, the breaker index, H/h, showed a minimum value of 0.203 and a maximum of 0.500, which implied that the waves were not limited by water depth. Moreover, the value of the depth to wavelength ratio of $h/\lambda = 0.159$ used in this campaign was far from the range of shallow waters ($h/\lambda < 0.05$), where shoaling phenomenon may occur and the treatment should account for a certain foreshore influence.

The Ursell number (Equation (7)) is a dimensionless number calculated as the quotient of the nonlinear term of finite height and the linear term of small height of the analytical solution of the wave elevation [45] and it is defined as:

$$Ur = H\lambda^2/h^3 \tag{7}$$

The Ursell number provides ranges of validity for different wave approximation methods. In cases where the Ursell number is low, $Ur \ll 1$, simplified linear wave theory can be applied. However, the Ursell number range for this experimental campaign was between 3.85 and 23.36. For this range of the Ursell number, the second order Stokes' wave theory could be applied according to the validity limit given by:

$$Ur < \frac{8\pi^2}{3} \cong 26.3 \tag{8}$$

This is the reason why Stokes' wave theory was implemented in the initial and boundary conditions of the computational model instead of the Airy linear theory.

The overtopping discharge was computed as the mean volumetric flow rate that crossed the vertical cross-sectional plane over the crest of the structure containing the axis of the cylinder, normal to the advancing direction of the wave. For the sake of direct comparison with the base case, the region of the plane above the diameter of the cylinder was considered, without including the extension caused by the addition of the parapet, which was assumed to be a non-usable portion of the top horizontal platform. The instantaneous volumetric flow rate crossing the region was integrated, yielding the total volume V_o. An example of a computational test can be observed in Figure 4.

The values for the mean overtopping flow rate Q and the corresponding mean overtopping discharge q were determined by taking into account the total time interval Δt when water overtopped the structure and the cylinder diameter, D, as:

$$q = \frac{Q}{D} = \frac{V_o}{\Delta \mathrm{t} \cdot D} \tag{9}$$

Then, this value was nondimensionalised in search of generalisation by using wave height H to obtain the relative overtopping discharge $\left(q/\sqrt{gH^3}\right)$.

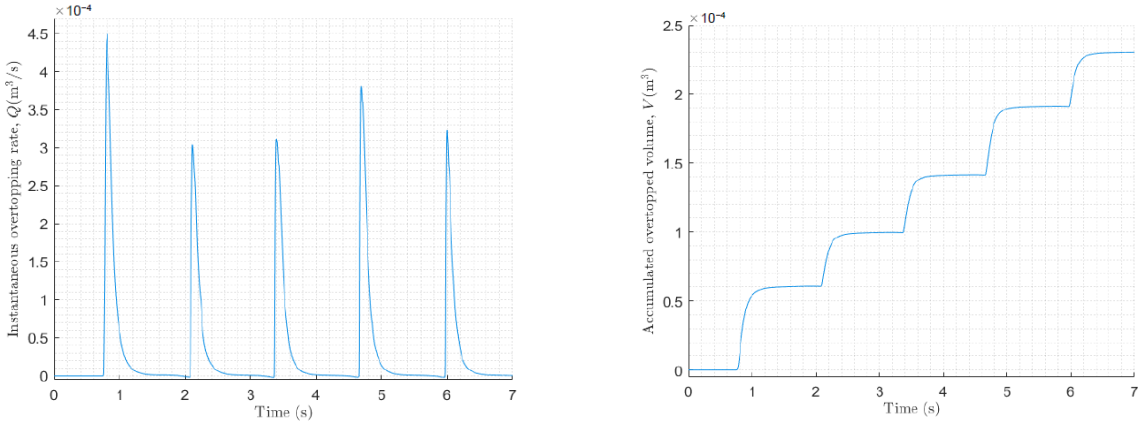

(**a**) (**b**)

Figure 4. Exported flow rate signals: (**a**) instantaneous flow rate, (**b**) accumulated overtopped volume. (Case: R_c/H = 0.538, H = 0.13 m, Geometry 4).

In addition, the evolution flow thickness δ with time was determined at the centre of the top surface of the cylinder (Figure 5). The mean value was computed afterwards by integration (Equation (6)). For both analyses, a time interval Δt of 5 periods, implying 5 overtopping events, were computed for all cases.

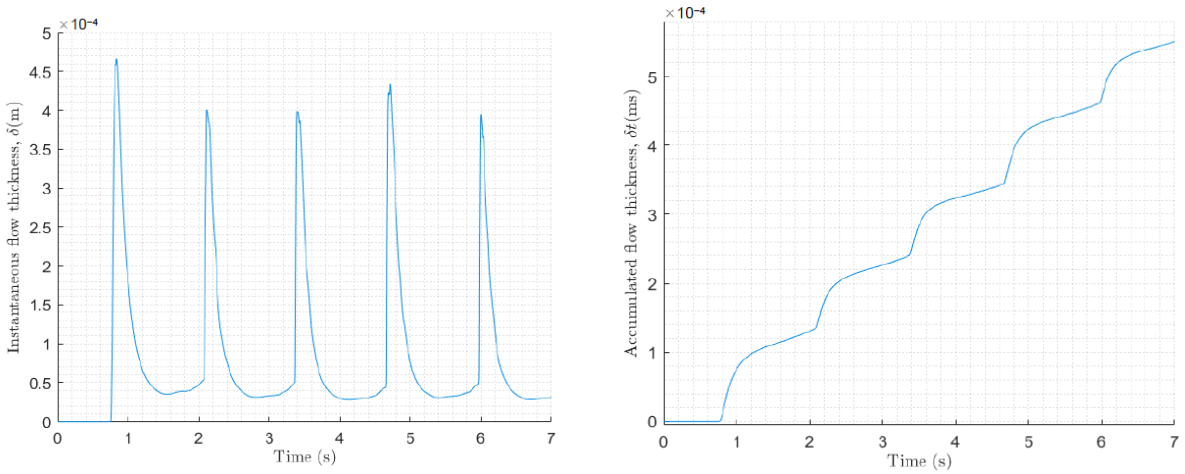

(**a**) (**b**)

Figure 5. Exported flow thickness signals: (**a**) instantaneous flow thickness, (**b**) integrated value over time. (Case: R_c/H = 0.538, H = 0.13 m, Geometry 4).

The definition of the relationship between the overtopping water volume and the overtopping flow thickness may enable experimental determination of overtopping without using a specific device to accumulate and read the overtopped water volume by employing wave probes located on top of the main structure.

3.2. Numerical Model

The commercial software STAR CCM+ (v17.02) was used to create and implement the numerical model, which was an application of the finite volume method, where the computational field was divided in small cells and flow equations were numerically solved for each cell.

3.2.1. Governing Equations

This section covers the conservation equations that were numerically applied to each cell. The specific model solved the mass conservation equation for an incompressible fluid, where there was no time derivative term attributed to variable density:

$$\frac{\partial U_i}{\partial x_i} = 0 \tag{10}$$

In addition, the conservation of momentum was addressed through the Reynolds-averaged Navier–Stokes equation:

$$\frac{\partial U_i}{\partial t} + \frac{\partial (U_i U_j)}{\partial x_j} = \frac{1}{\rho}\frac{\partial}{\partial x_j}\left(-p\delta_{ij} + 2\mu S_{ij} - \rho\overline{u_i' u_j'}\right) + F_i + S_i \tag{11}$$

$$S_{ij} = \frac{1}{2}\left(\frac{\partial U_i}{\partial x_j} + \frac{\partial U_j}{\partial x_i}\right) \tag{12}$$

where $i, j = 1, 2, 3$ are the subscripts of the three Cartesian components, U_i is the ith time-averaged velocity component and u_i' is the pulsations of the velocity component resulting from turbulence. ρ is fluid density, δ_{ij} is the Kronecker delta function, p is the pressure, F_i stands for the ith component of the external field force per unit mass (in this case the weight of the fluid) and S_i is a specific sink or source of the ith component of momentum if needed. S_{ij} stands for the viscous tensor defining the shear stress components coming from average velocity gradients for an incompressible flow.

The additional viscous terms coming from the pulsating velocity components characteristic of the turbulent behaviour can be associated with the main flow pattern and its averaged velocities, following the Boussinesq hypothesis for incompressible flow:

$$-\rho\overline{u_i' u_j'} = \mu_t\left(\frac{\partial U_i}{\partial x_j} + \frac{\partial U_j}{\partial x_i}\right) - \frac{2}{3}\rho k_t \delta_{ij} \tag{13}$$

where μ_t is the eddy viscosity and $k_t = \frac{1}{2}\overline{u_i' u_i'}$ is the turbulent kinetic energy. The new term on right of the Equation (13) was included to make the Boussinesq definition valid when all three terms of the diagonal of the turbulent tensor were added in $-\rho\overline{u_i' u_i'}$. These, μ_t and k_t, were two new parameters characteristic of the turbulent flow that can be derived from a turbulent model. The selected model was the standard low-Re K-epsilon, which added two new transport equations for the evaluation of the two unknowns, as described in detail in [40].

As for phase interaction, the case studied in this campaign involved very large masses or parcels of fluid of each fluid with a very well defined interface due to the nature of non-impulsive non-breaking waves. These simple conditions were appropriately represented by the volume of fluid (VOF) method [13], stating the conservation of phases:

$$\frac{\partial \alpha}{\partial t} + \nabla \cdot \left(\alpha \vec{U}\right) = 0 \tag{14}$$

where α represents the volume fraction of water and $(\alpha - 1)$ is the volume fraction of air. The material properties of density and dynamic viscosity were computed by a weighted average:

$$\rho = \alpha\rho_{water} + (1 - \alpha)\rho_{air} \tag{15}$$

$$\mu = \alpha\mu_{water} + (1 - \alpha)\mu_{air} \tag{16}$$

3.2.2. Computational Domain and Boundary Conditions

The computational field (Figure 6) was the reference configuration of the base case defined in [40]. It consisted of a parallelepiped 0.3 m wide, 0.7 m high and 5 wavelengths long. The length of the domain was subdivided into three zones: one wavelength upstream of the cylinder and three wavelengths downstream of the cylinder, where a damping model was applied at the final two wavelengths. The width of 0.3 m represented one half of the total width of the flume because a symmetry plane condition was applied at the middle plane (i.e., only one symmetric half of the problem was simulated). This size of 0.6 m guaranteed that the transversal horizontal dimension was wide enough in comparison with the diameter of the cylinder of 0.11 m (larger than 5:1) to neglect the effects of the lateral walls of the flume in the wave–structure interaction [46].

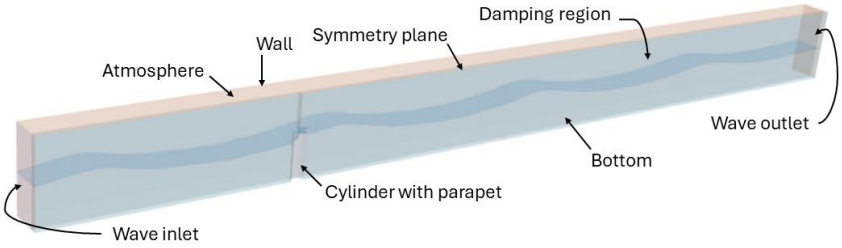

Figure 6. Computational domain of the numerical model.

Regarding the boundary conditions, a non-slipping impermeable wall condition was used for all the surfaces of the cylinder and the parapet, and for the side surface and the bottom of the flume. A constant pressure outlet at atmospheric pressure was defined for the top surface.

Regarding wave generation, a velocity inlet boundary was defined at the position of the wave inlet on the left-hand side of the numerical flume according to the theory of high-order Stokes that defines the free surface elevation $\eta(x, t)$, the velocity potential (x, z, t) and the pressure field [47]. The velocity field there was defined from the velocity potential as $U_i = \frac{\partial \phi}{\partial x_i}$. At the wave outlet section, on the right-hand side of the numerical flume, the hydrostatic pressure due to the water column was imposed in addition to the upstream damping region to prevent wave reflection. The details of the corresponding equations affecting the wave inlet, wave outlet and damping region are presented in [40].

3.2.3. Mesh

The meshing models used to discretise the wave flume were based on hexahedral cells in the whole volume (except the regions close to curved surfaces). The base size of the cells in the flume was 0.075 m for those regions far from regions showing pressure and velocity gradients. More refined cells were used near the free surface to capture the wave propagation and, in the surroundings of the cylinder, the parapet and the region above the crest where overtopping phenomenon had the greatest impact in the modification of the fluid flow pattern (Figure 7). The total number of cells in the meshing model amounted to an average of $1.25 \cdot 10^6$ cells. The specific refinement for each region is stated in Table 3.

Table 3. Hexahedral mesh refinement.

	Δx/λ	**Δy/λ**	**Δz/λ**
Region 1	1/150	1/150	1/300
Region 2	1/75	1/75	1/150
Region 3	1/300	1/300	1/1200

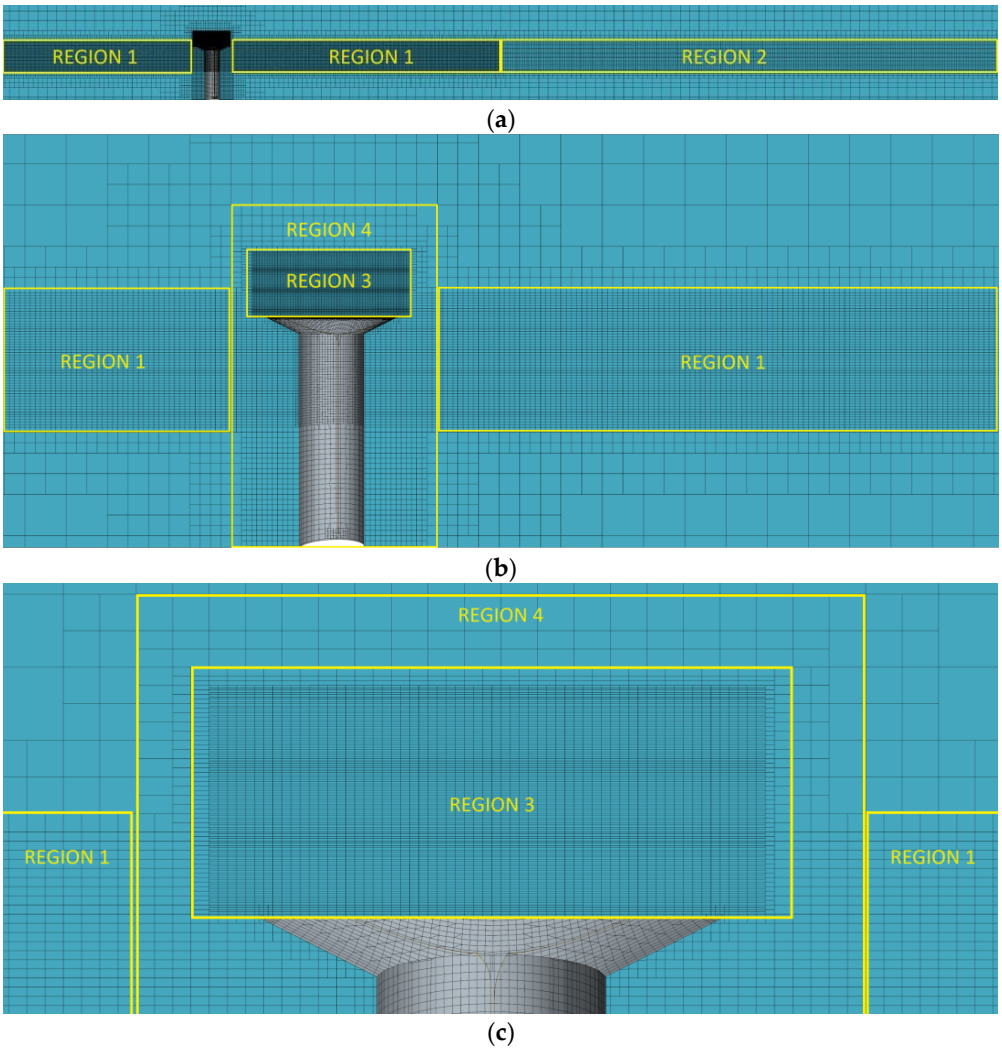

Figure 7. Mesh of the numerical wave flume: (**a**) general overview, (**b**) detailed view around the cylinder and the parapet and (**c**) detailed view above the crest.

More specifically, there were four different zones with higher resolutions corresponding to the free surface range of the first half of the tank (region 1), which included the wave generation and the wave propagation after the overtopping phenomenon; the free surface range of the second half of the tank (region 2), where wave damping was imposed; the volume directly on top of the cylinder (region 3), where overtopping was measured; and the volume surrounding the vertical cylinder (region 4), the volume where waves interacted with the cylinder. As for the mesh in region 4, a variable mesh size with a maximum base size corresponding to 1/8 of the base size of the flume (0.075 m) was selected; its objective was to both correctly mesh the cylinder perimeter and to expand isotropically and radially to fit with the other meshing regions. Mesh definition was chosen so that numerical damping had little to no effect on the waves that were created. The requirements for the damping zone were not as strict and the mesh thus included half the cells per wavelength in all three directions. Moreover, it has been proven that a larger cell size improves damping because it increases numerical dissipation [48].

The time step size, which separated each successive time iteration, was chosen to ensure it satisfied the Courant–Friedrichs–Lewy condition. This selection was based on the dimensions of the cells and the waves' celerity. A maximum Courant number of 0.33 was permitted. This choice, coupled with a second-order temporal discretisation, resulted in a well-defined interface between the two phases and effectively mitigated any undesirable

smearing effects because of numerical diffusion and the typical smearing effect in the definition of the interface.

3.2.4. Initial Conditions

The initial conditions of the simulations were given by the interphase location, fluid velocity and pressure distributions. The initial position of the waves (Figure 8) were defined such that there was a wave trough placed at the cylinder axis, helping the convergence of the solution from the first iteration.

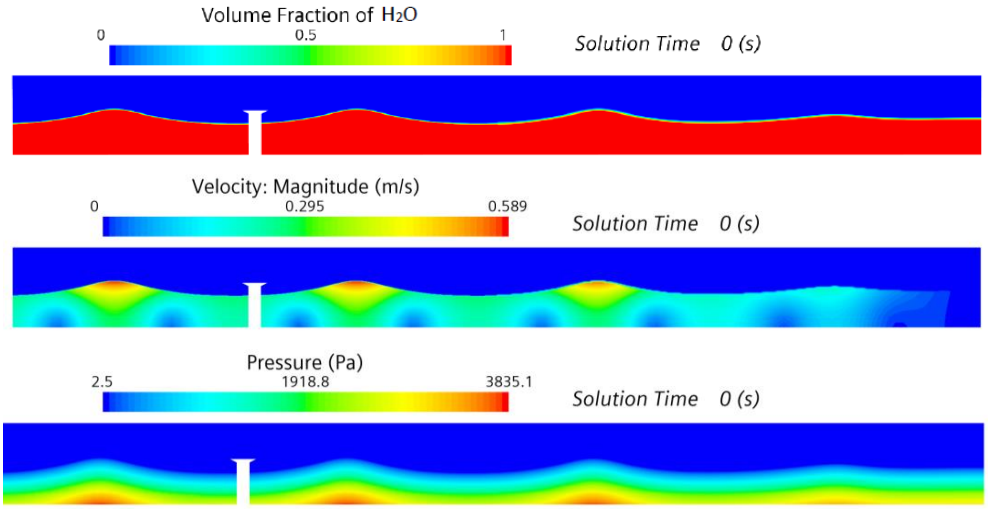

Figure 8. Initial conditions for free surface (**top**), velocity (**middle**) and pressure contours (**bottom**).

4. Results and Discussion

All 96 cases defined in Section 3 were computed with the numerical model described in the previous section. As an example of an individual run, some snapshots of the scalar water volume fraction were presented at different times of an overtopping event to compare the progress of the wave over the crest of the cylinder with and without parapet (Figure 9). An example of the quantitative computation of the evolution of the overtopping flow discharge and flow thickness with time is presented in Figure 10 for both cases.

The different behaviour of the continuous layer of water flowing over the crest of the cylinder, known as green water contribution, was noticed when comparing situations without (a–c) and with parapet (d–f), as shown in Figure 9. The parapet induced a change in the direction of the flow by diverting it backwards and laterally outwards during the run-up process, leading to a net reduction of the overtopped volume over the crest. The evolution of the computed overtopping discharge with time (Figure 10) for this particular case showed a net reduction greater than 20% in the peak values of the discharge and greater than 30% in the peak value of the flow thickness.

All the data obtained using the numerical model in each test, as in the particular case presented above, were fitted to have an analytical expression representative of the overtopping behaviour characteristic of the specific geometry. Given the non-impulsive regime of the experiment and the lack of influence by the foreshore, the relative overtopping rate could be evaluated with a Weibull-type Formula (2). More specifically, given the regime of studied parapets, the relative overtopping rate data were fitted using a piecewise Equation (5) by taking into account the two lower relative freeboards of the three different overtopping regimes occurring with parapets. The value of 0.5 for the relative freeboard was preserved to establish the change from the low relative freeboard regime to the intermediate relative freeboard regime. The tendencies resulting from the fitting process to the overtopping data of each of the four different geometrical modifications of the vertical cylinder can be observed in Figure 11, together with the corresponding coefficient of determination. The corresponding fitting parameters are presented in Table 4.

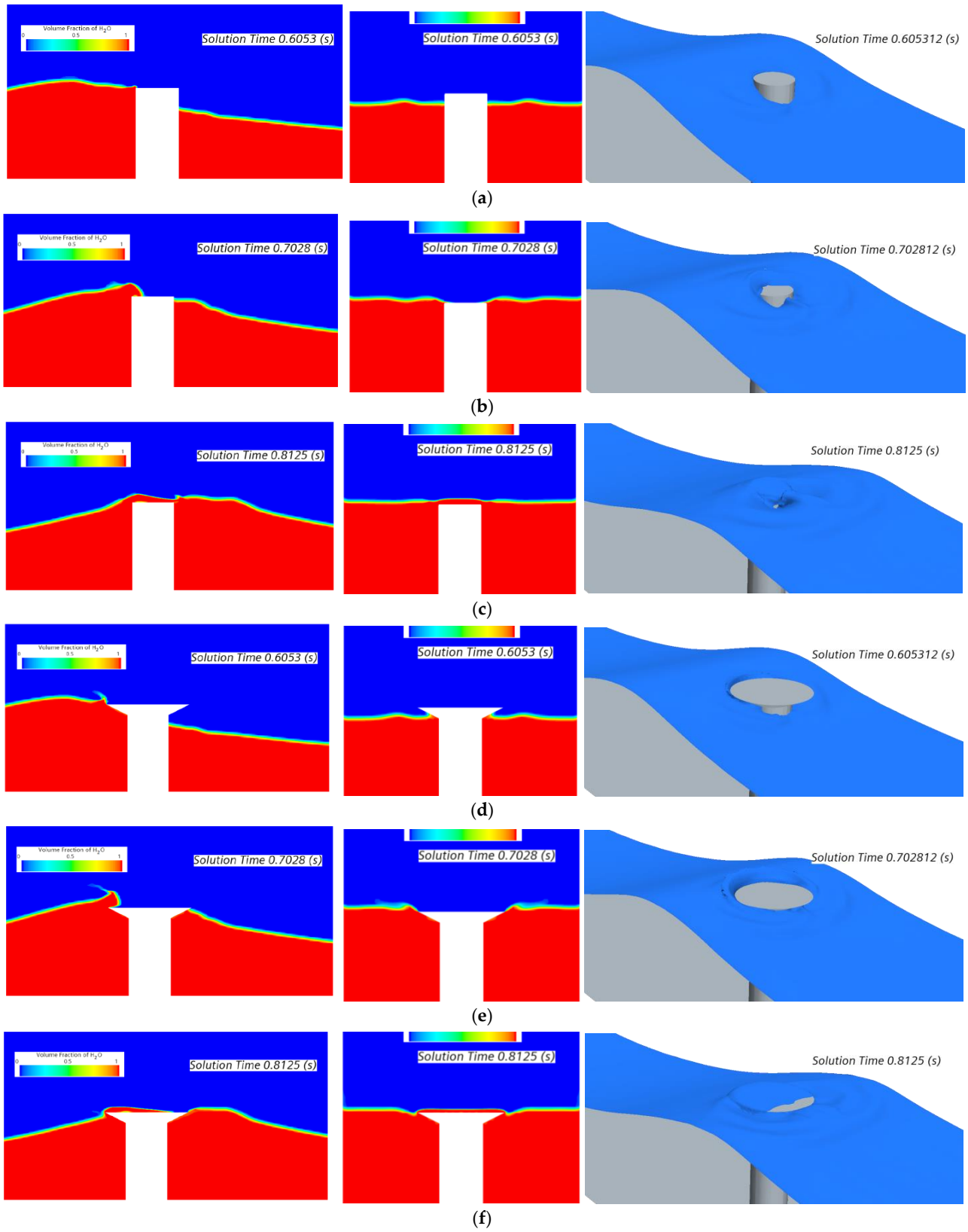

Figure 9. Volume fraction of water at the symmetry plane and free surface shape evolution with time: (**a**–**c**) plain cylinder and (**d**–**f**) cylinder with parapet. Left: longitudinal symmetry plane; bottom: transversal symmetry plane; right: 3D view. (Relative freeboard R_c/H = 0.538, height H = 0.13 m, parapet geometry 4).

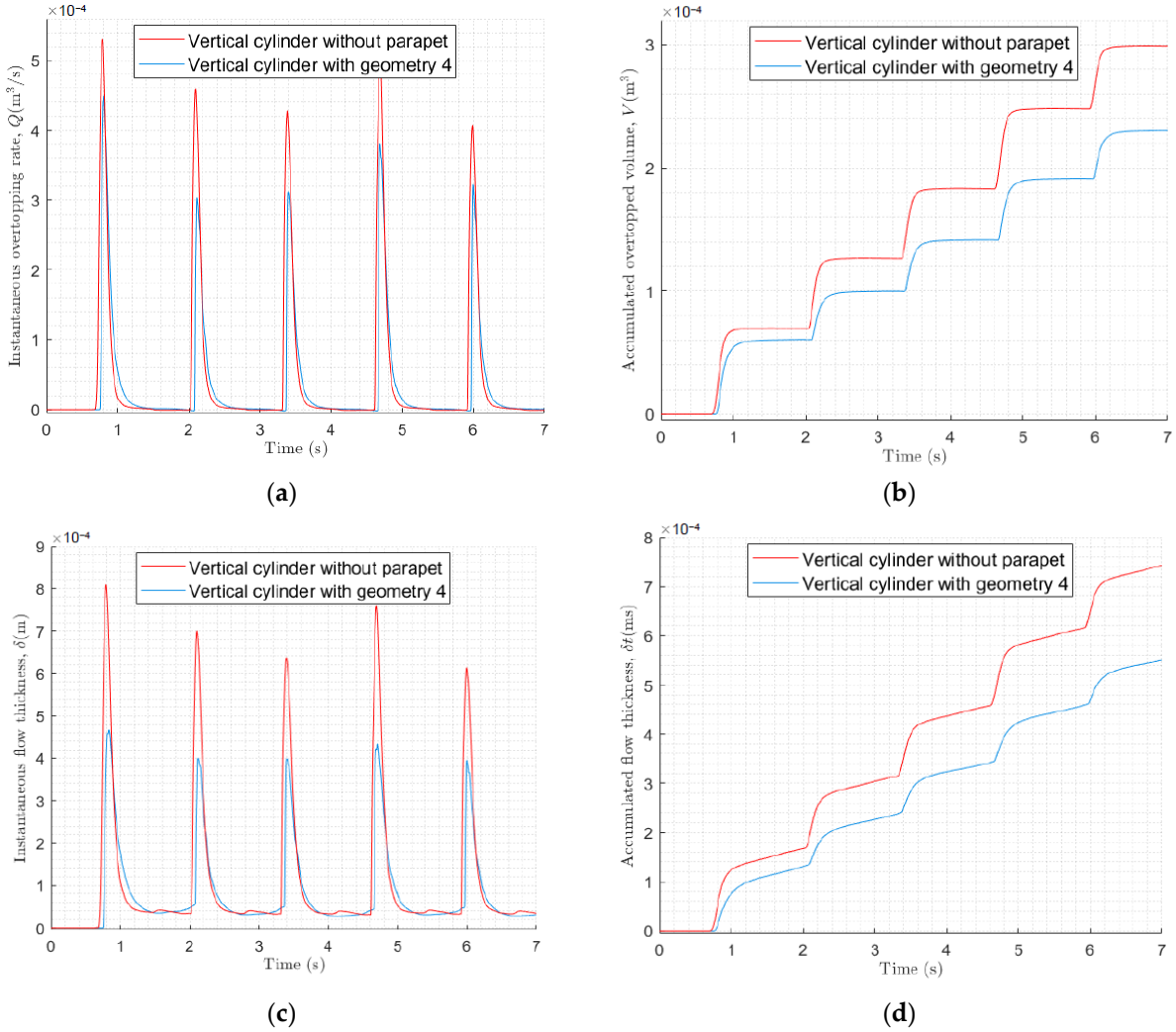

Figure 10. Comparison of the evolution of the overtopping phenomenon with time for a cylinder with and without parapet: (**a**) instantaneous overtopping discharge, (**b**) accumulated overtopped volume, (**c**) instantaneous flow thickness and (**d**) flow thickness integrated over time. (Relative freeboard R_c/H = 0.538, height H = 0.13 m, parapet geometry 4).

Table 4. Fitting parameters of the piecewise Weibull equation for each geometry.

	a	b	c	d	e	f
Geometry 1	0.0449	3.07	1.9	0.0062	1.74	6.9
Geometry 2	0.0703	4.74	1.1	0.0051	1.73	7.8
Geometry 3	0.0578	3.85	1.3	0.0066	1.79	6.2
Geometry 4	0.0543	3.76	1.4	0.0048	1.71	8.2

The overtopping reduction resulting from the four parapet options followed a similar pattern, with a moderate reduction in the low relative freeboard regime, which became very pronounced in the intermediate relative freeboard regime ($R_c/H > 0.5$). If we compare the results obtained for the four geometries in the same graph (Figure 12a), one can observe that Geometries 2 and 4 were slightly better than Geometries 1 and 3, pointing out the advantage of using a ratio of the height of the parapet to its horizontal extension of h_r/B_r = 0.5 over the value of 1.0. In addition, the increase by one-third (33%) of the lengths of the parapet when comparing Geometry 1 with Geometry 3 or, separately, Geometry 2 with Geometry 4 did not lead to any significant variation in the overtopping.

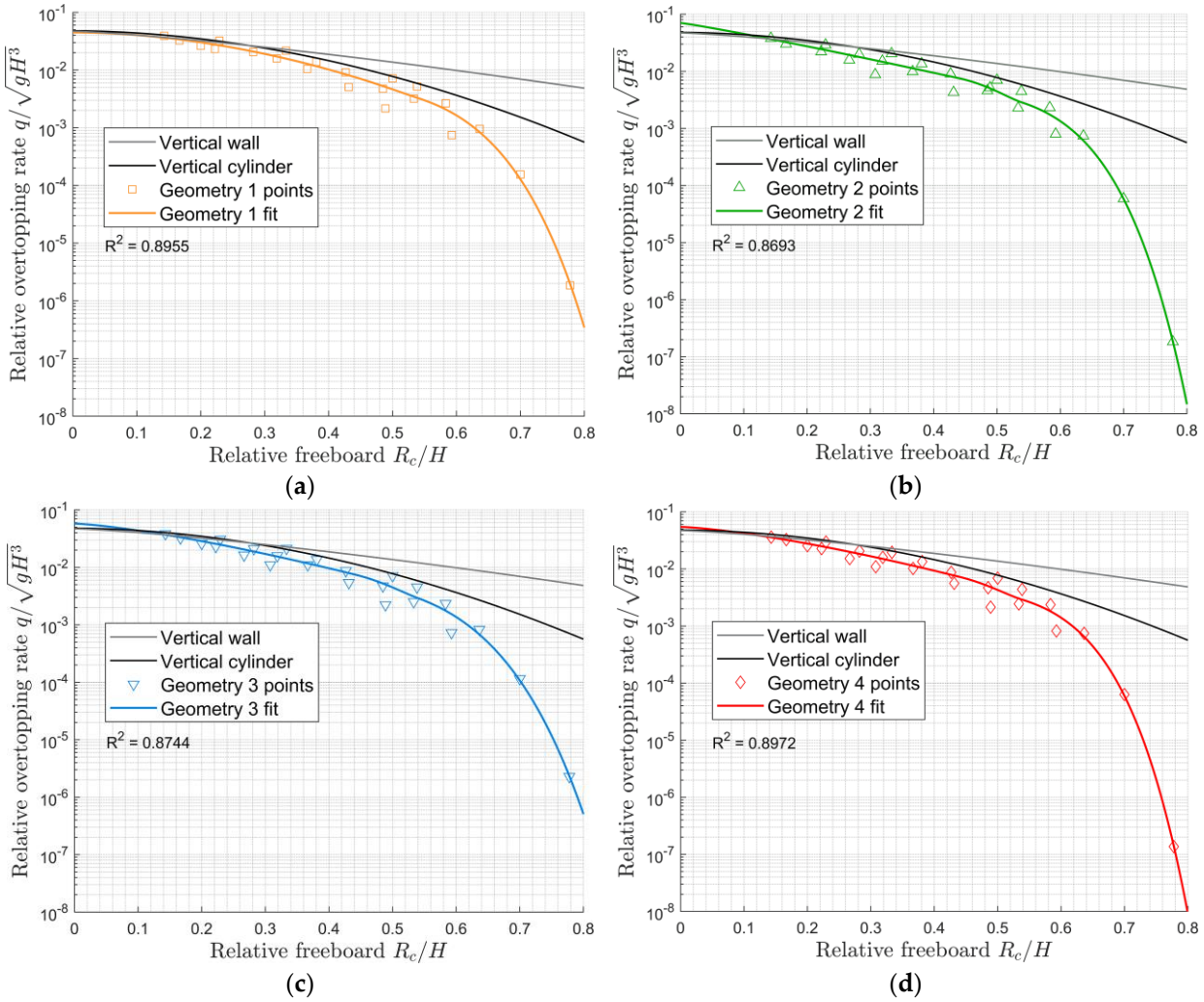

Figure 11. Relative overtopping rate as a function of relative freeboard of the parapet geometries: (**a**) Geometry 1, (**b**) Geometry 2, (**c**) Geometry 3 and (**d**) Geometry 4.

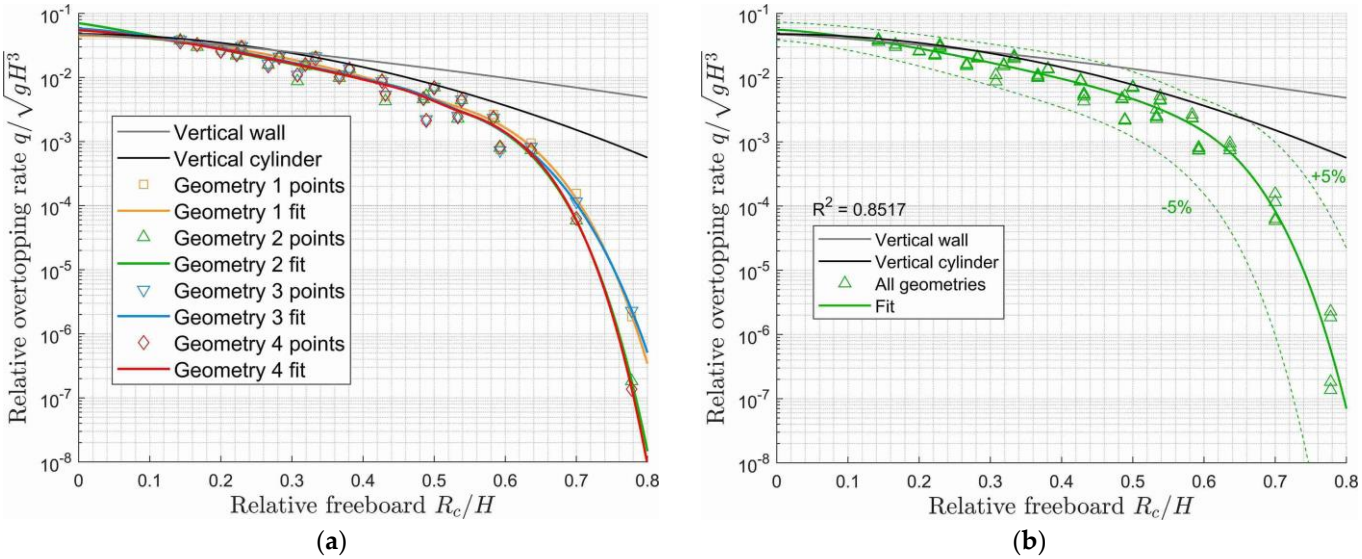

Figure 12. Relative overtopping rate as a function of relative freeboard: (**a**) different regressions for each geometry; (**b**) common regression for all geometries.

However, one should bear in mind that the inherent dispersion in the data sets of the numerically predicted overtopping rate was very significant in this type of test due to the highly nonlinear nature of the overtopping phenomenon and the increasingly high statistical uncertainty of the overtopping discharge for higher relative freeboards with smaller overtopping. Thus, the previously addressed distinctive behaviour fell well within the admitted statistical uncertainty if a common unique regression was used for the four geometries (Figure 12b). The corresponding dispersion resulting from the fitting procedure was performed according to very well-established standards in the field [21]. The covariance matrix of the fitting constants was used to define the bounding curves containing the data with a certain confidence level. Assuming that the uncertainty of the fitted parameters followed a normal distribution, the exceedance lines were calculated as $a_i + 1.64 \cdot \sigma$ and $a_i - 1.64 \cdot \sigma$, with a_i being the ith fitting parameter and σ its standard deviation. This was equivalent to using a 90% confidence interval band in the calculation of the fitting parameters.

The resulting Weibull piecewise expression representing the overtopping reduction for cases $h_r/B_r \in [0.5, 1]$ from the fitting to the individual computational points (Figure 12b) was as follows:

$$\frac{Q}{\sqrt{gH^3D}} = \begin{Bmatrix} 0.0558 \cdot \exp\left[-\left(3.76\frac{R_c}{H}\right)^{1.4}\right], & \frac{R_c}{H} \leq 0.5 \\ 0.00544 \cdot \exp\left[-\left(1.73\frac{R_c}{H}\right)^{7.4}\right], & \frac{R_c}{H} > 0.5 \end{Bmatrix} \quad (17)$$

The coefficient of determination of this unique regression line showed a reasonable value of $R^2 = 0.8517$ and all the points were well withing the range of 90% confidence interval.

The uncertainty of each fitting parameter is given in Table 5.

Table 5. Fitting parameters of each geometry.

a	b	c	d	e	f
0.0558	3.76	1.4	0.00544	1.73	7.4
σ(a)	**σ(b)**	**σ(c)**	**σ(d)**	**σ(e)**	**σ(f)**
0.0107	0.586	0.29	0.00231	0.0853	1.1

Figure 13 shows a good correlation of the individual computational results with the corresponding values given by the previous regression line defined in Equation (17), where all the points fell inside the band, limiting the range of 10 times and 0.1 times the calculated values.

As far as the mean flow thickness $\overline{\delta}$ was concerned, the individual cases obtained by computing the individual signals (Figure 10c,d) coming from all the tests and geometries were analysed with a non-dimensional approach. The overall tendency of the non-dimensional flow thickness $\overline{\delta}/H$ generated by the overtopping phenomenon followed a marked exponential dependency on the relative freeboard R_c/H (Figure 14). In the same way as for the overtopping discharge, it was difficult to distinguish between the phenomenon generated by the different parapet geometries (Figure 14a), and the use of a unique expression resulted in being a reasonable approach, where the majority of the numerical results fell within the 5% exceedance band.

Here, the direct relationship between the relative average flow thickness and the relative freeboard suggested in [40] by following an exponential tendency was certified:

$$\frac{\overline{\delta}}{H} = 0.1515 \cdot \exp\left(-4.16\frac{R_c}{H}\right) \quad (18)$$

This fitting expression showed a reasonable value of the coefficient of determination of $R^2 = 0.9661$.

It can be observed how the parapet-type mitigation structure induced a net reduction of the flow thickness in comparison with the plain cylinder. The quantitative reduction could be evaluated by simultaneous consideration with the flow thickness attributed to the cylindrical case, with no influence of foreshore and non-impulsive conditions [37]:

$$\frac{\overline{\delta}}{H} = 0.1769 \cdot \exp\left(-4.11 \frac{R_c}{H}\right) \tag{19}$$

This result confirmed the viability of deriving the overtopping reduction by computing the reduction of the flow thickness [40]. In Figure 15, a direct linear relationship between the two variables is very well correlated.

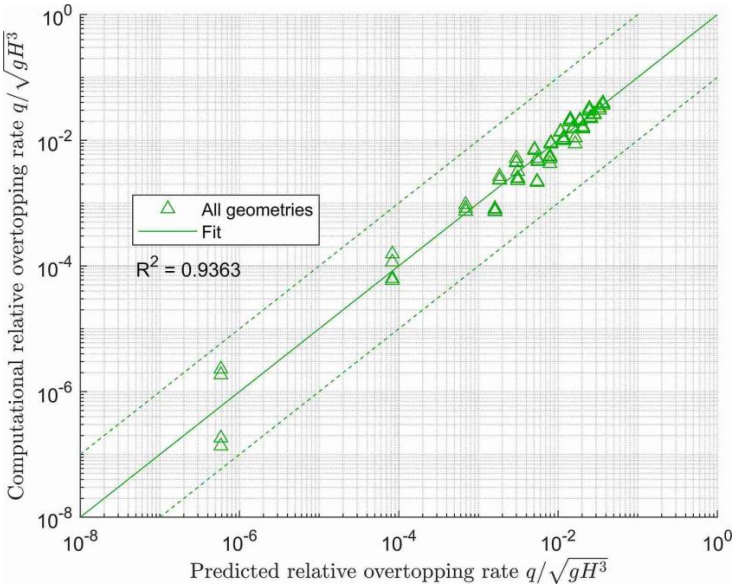

Figure 13. Correlation between computational and estimated results of the overtopping rate.

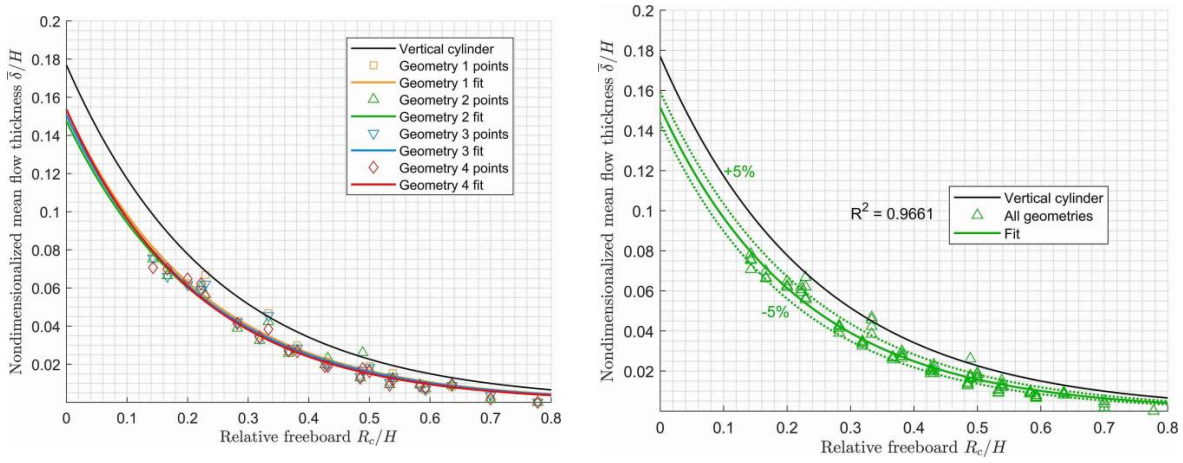

(**a**) (**b**)

Figure 14. Nondimensionalised mean flow thickness as a function of relative freeboard of the different parapet geometries (**a**) and overall tendency (**b**).

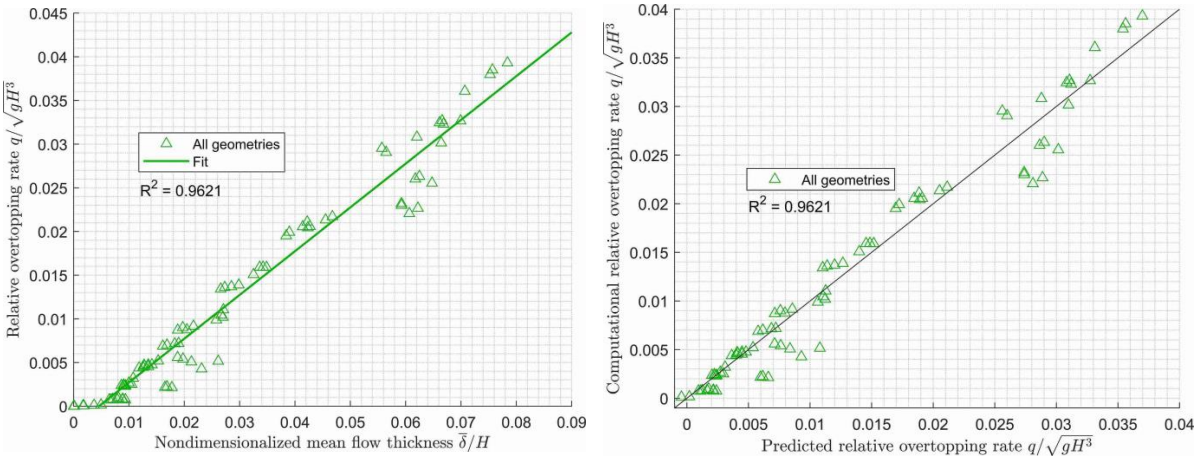

(**a**) (**b**)

Figure 15. Dependence of the relative overtopping rate on the nondimensionalised mean flow thickness: (**a**) fitting line and (**b**) quality of the fitting.

The relationship between nondimensionalised flow thickness and relative overtopping rate in this case was:

$$\frac{Q}{\sqrt{gH^3D}} = -0.00229 + 0.5009 \cdot \frac{\bar{\delta}}{H} \quad (20)$$

Here, in the linear regression, a negative independent term was allowed (Figure 15a), addressing the fact that, even at a very low overtopping discharge close to zero, a certain water layer existed over the crest with very low flow velocity. This effect could be noticed by simultaneously analysing the flow thickness and the corresponding overtopping rate, as shown in Figure 10. The correlation of the predicted values by linear regression with the corresponding values coming from the numerical calculation was reasonably acceptable (Figure 15b), with a coefficient of determination of $R^2 = 0.9661$, by taking into account the high dispersion attributed to this type of phenomenon.

5. Conclusions

In the present study, a computational model was used to characterise the overtopping reduction produced by different geometric options of overtopping mitigation structures installed at the top of a reference fixed cylinder. The selected mitigation structure was a parapet with a variable height to extension ratio of $h_r/B_r \in [0.5, 1]$.

The computational model followed the same configuration used to characterise a plane cylinder in previous research, which was used as the basis of the present study. The wave characteristics were the same as for the reference cylinder, belonging to the non-impulsive regime without influence of the foreshore in the intermediate water depth range.

A total of 96 individual computational cases were run with four different parapets, with different relative freeboard values ranging from 0.143 to 0.778. In the same way as for linear defence vertical walls, the inclusion of a parapet led to a comparative net reduction of the overtopping discharge, and the result was successfully modelled by a Weibull piecewise function. This expression reported that the overtopping reduction produced by the parapet became very noticeable in the intermediate relative freeboard regime, for values of $R_c/H > 0.5$.

The nondimensionalised mean flow thickness was calculated at the centre of the crest of the structure by indicating a direct relationship with the overtopping discharge. This flow thickness parameter was reduced in relation to the reference cylinder without a parapet when comparing the same relative freeboard cases. A direct relationship between the nondimensionalised mean flow thickness and the relative overtopping rate was determined, showing a good alternative of indirect estimation of the overtopping discharge without needing a complex quantification of overtopped volume in real full scale structures.

Among the different geometric options, the selection of greater parapet extension B_r in comparison with the parapet height h_r seemed to produce a slightly higher performance in overtopping reduction. However, this difference did not prove a meaningful distinction considering the statistical dispersion of the results, and a unique formulation was attributed to the group of parapets considered in this study.

This study may be considered the basis for future characterisation of the overtopping phenomenon in a more complex environment where cylindrical components used in floating offshore structures are exposed to extreme waves and, as a consequence, moving with the six degrees of freedom but constrained by the mooring system at the same time.

Author Contributions: Conceptualisation, methodology and supervision, G.A.E.; software, investigation, data curation and writing—original draft preparation, X.E.; formal analysis, X.E. and G.A.E.; resources and visualisation, I.B. and I.A.; writing—review and editing G.A.E. and U.I.; project administration, G.A.E. and U.I. All authors have read and agreed to the published version of the manuscript.

Funding: This work was carried out within the framework of the ITSAS-REM Research Group (IT-1514-22) funded by the Basque Government.

Acknowledgments: Technical and human support provided by IZO-SGI, SGIker (UPV/EHU, MICINN, GV/EJ, ERDF and ESF) is gratefully acknowledged, as along with the support provided by the Joint Research Laboratory on Offshore Renewable Energy (JRL-ORE).

Conflicts of Interest: The authors declare no conflict of interest.

References

1. Tagliafierro, B.; Karimirad, M.; Altomare, C.; Göteman, M.; Martínez-Estévez, I.; Capasso, S.; Domínguez, J.M.; Viccione, G.; Gómez-Gesteira, M.; Crespo, A.J.C. Numerical Validations and Investigation of a Semi-Submersible Floating Offshore Wind Turbine Platform Interacting with Ocean Waves Using an SPH Framework. *Appl. Ocean Res.* **2023**, *141*, 103757. [CrossRef]
2. Zhang, Y.; Xu, H.; Law, Y.; Santo, H.; Magee, A. Hydrodynamic Analysis and Validation of the Floating DeepCwind Semi-Submersible under 3-h Irregular Wave with the HOS and CFD Coupling Method. *Ocean Eng.* **2023**, *287*, 115701. [CrossRef]
3. Zhou, Y.; Xiao, Q.; Liu, Y.; Incecik, A.; Peyrard, C.; Li, S.; Pan, G. Numerical Modelling of Dynamic Re-sponses of a Floating Offshore Wind Turbine Subject to Focused Waves. *Energies* **2019**, *12*, 3482. [CrossRef]
4. van der Meer, J.W.; Verhaeghe, H.; Steendam, G.J. The new wave overtopping database for coastal structures. *Coast. Eng.* **2009**, *56*, 108–120. [CrossRef]
5. Pullen, T.; Allsop, N.W.H.; Bruce, T.; Kortenhaus, A.; Schüttrumpf, H.; van der Meer, J.W. *Eurotop, Wave Overtopping of Sea Defences and Related Structures: Assessment Manual*; Kuratorium für Forschung im Küsteningenieurwesen, Boyens Medien GmbH & Co. KG,: Heide im Holstein, Germany, 2007.
6. Van der Meer, J.W.; Allsop, N.W.H.; Bruce, T.; De Rouck, J.; Kortehaus, A.; Pullen, T.; Schümpttrumpf, H.; Troch, P.; Zanuttigh, B. EurOtop Manual on Wave Overtopping of Sea Defences and Related Structures an Overtopping Manual Largely Based on European Research, But for Worldwide Application, 2nd ed. 2018. Available online: www.overtopping-manual.com (accessed on 10 August 2024).
7. Izquierdo, U.; Esteban, G.A.; Blanco, J.M.; Albaina, I.; Peña, A. Experimental validation of a CFD model using a narrow wave flume. *Appl. Ocean Res.* **2019**, *86*, 1–12. [CrossRef]
8. Chen, X.; Hofland, B.; Altomare, C.; Suzuki, T.; Uijttewaal, W. Forces on a vertical wall on a dike crest due to overtopping flow. *Coast. Eng.* **2015**, *95*, 94–104. [CrossRef]
9. Lu, X.; Zhou, G.G.D.; Cui, K.F.E.; Tang, H.; Xie, Y. Overtopping volume of impulse waves in glacier lakes: Experimental and numerical investigation using rigid dams. *Eng. Geol.* **2022**, *306*, 106763. [CrossRef]
10. Wuppukondur, A.; Baldock, T.E. Physical and numerical modelling of representative tsunami waves propagating and overtopping in converging channels. *Coast. Eng.* **2022**, *174*, 104120. [CrossRef]
11. Zago, V.; Dalrymple, R.A.; Almashan, N.; Bilotta, G.; Al-Houti, D.; Neelamani, S. Characterization and modeling of greenwater overtopping of a sea-level deck. *Ocean Eng.* **2023**, *275*, 114131. [CrossRef]
12. Dang, B.L.; Nguyen-Xuan, H.; Abdel Wahab, M. Numerical study on wave forces and overtopping over var-ious seawall structures using advanced SPH-based method. *Eng. Struct.* **2021**, *226*, 111349. [CrossRef]
13. Hirt, C.W.; Nichols, B.D. Volume of Fluid (VOF) Method for the Dynamics of Free Boundaries. *J. Comput. Phys.* **1981**, *39*, 201–225. [CrossRef]
14. van Bergeijk, V.M.; Warmink, J.J.; Hulscher, S.J.M.H. The effects of transitions in cover type and height on the wave overtopping load on grass-covered flood defences. *Appl. Ocean Res.* **2022**, *125*, 103220. [CrossRef]
15. Buccino, M.; Di Leo, A.; Tuozzo, S.; Còrdova Lopez, L.F.; Clabrese, M.; Dentale, F. Wave overtopping of a vertical seawall in a surf zone: A joint analysis of numerical and laboratory data. *Ocean Eng.* **2023**, *288*, 116144. [CrossRef]

16. Sharifian, M.; Moghim, M.N.; Chamani, M.R. Numerical simulation of waves overtopping over impermeable sloped seadikes. *Ocean Eng.* **2022**, *266*, 113100. [CrossRef]
17. Stagnitti, M.; Lara, J.L.; Musumeci, R.E.; Foti, E. Numerical modeling of wave overtopping of damaged and up-graded rubble-mound breakwaters. *Ocean Eng.* **2023**, *280*, 114798. [CrossRef]
18. Irías Mata, M.; van Gent, M.R.A. Numerical modelling of wave overtopping discharges at rubble mound breakwaters using OpenFOAM®. *Coast. Eng.* **2023**, *181*, 104274. [CrossRef]
19. Vanneste, D.F.A.; Altomare, C.; Suzuki, T.; Troch, P.; Verwaest, T. Comparison of numerical models for wave overtopping and impact on a sea wall. *Coast. Eng. Proc.* **2014**, *1*, 5. [CrossRef]
20. Zhou, M.; Shi, Z.; Peng, C.; Peng, M.; Cui, K.F.E.; Li, B.; Zhang, L.; Zhou, G.G.D. Two-phase modelling of erosion and deposition process during overtopping failure of landslide dams using GPU-accelerated ED-SPH. *Comput. Geotech.* **2024**, *166*, 105944. [CrossRef]
21. van der Meer, J.; Bruce, T. New Physical Insights and Design Formulas on Wave Overtopping at Sloping and Vertical Structures. *J. Waterw. Port Coast. Ocean Eng.* **2014**, *140*, 04014025. [CrossRef]
22. Zanuttigh, B.; Formentin, S.M.; van der Meer, J.W. Prediction of extreme and tolerable wave overtopping dis-charges through an advanced neural network. *Ocean Eng.* **2016**, *127*, 7–22. [CrossRef]
23. Zanuttigh, B.; Formentin, S.M. Reduction of the wave overtopping discharge at dikes in presence of crown walls with bullnoses. *Coast. Eng. Proc.* **2018**, *1*, 110. [CrossRef]
24. Formentin, S.M.; Palma, G.; Zanuttigh, B. Integrated assessment of the hydraulic and structural performance of crown walls on top of smooth berms. *Coast. Eng.* **2021**, *168*, 103951. [CrossRef]
25. Van Doorslaer, K.; De Rouck, J. Wave overtopping over sea dikes and impact forces on storm walls. In Proceedings of the Ninth International Conference on Coastal and Port Engineering in Developing Countries—PIANC COPEDEC IX, Río de Janeiro, Brazil, 16–21 October 2016.
26. Van Doorslaer, K.; Romano, A.; De Rouck, J.; Kortenhaus, A. Impacts on a storm wall caused by non-breaking waves overtopping a smooth dike slope. *Coast. Eng.* **2017**, *120*, 93–111. [CrossRef]
27. Martinelli, L.; Ruol, P.; Volpato, M.; Favaretto, C.; Castellino, M.; De Girolamo, P.; Franco, L.; Romano, A.; Sammarco, P. Experimental investigation on non-breaking wave forces and over-topping at the recurved parapets of vertical breakwaters. *Coast. Eng.* **2018**, *141*, 52–67. [CrossRef]
28. Castellino, M.; Sammarco, P.; Romano, A.; Martinelli, L.; Ruol, P.; Franco, L.; De Griloamo, P. Large impulsive forces on recurved parapets under non-breaking waves. A numerical study. *Coast. Eng.* **2018**, *136*, 1–15. [CrossRef]
29. Castellino, M.; Romano, A.; Lara, J.L.; Losada, I.J.; De Girolamo, P. Confined-crest impact: Forces dimensional analysis and extension of the Goda's formulae to recurved parapets. *Coast. Eng.* **2021**, *163*, 103814. [CrossRef]
30. Suzuki, T.; Altomare, C.; Veale, W.; Verwaest, T.; Trouw, K.; Troch, P.; Zijlema, M. Efficient and robust wave overtopping estimation for impermeable coastal structures in shallow foreshores using SWASH. *Coast. Eng.* **2017**, *122*, 108–123. [CrossRef]
31. van Gent, M.R.A.; Wolters, G.; Capel, A. Wave overtopping discharges at rubble mound breakwaters includ-ing effects of a crest wall and a berm. *Coast. Eng.* **2022**, *176*, 104151. [CrossRef]
32. Etemad-Shahidi, A.; Koosheh, A.; van Gent, M.R.A. On the mean overtopping rate of rubble mound structures. *Coast. Eng.* **2022**, *177*, 104150. [CrossRef]
33. Van Doorslaer, K.; De Rouck, J. Reduction on wave overtopping on a smooth dike by means of a parapet. *Coast. Eng. Proc.* **2011**, *1*, 6. [CrossRef]
34. Kortenhaus, A.; Pearson, J.; Bruce, T.; Allsop, N.W.H.; van der Meer, J.W. Influence of parapets and recurves on wave overtopping and wave loading of complex vertical walls. In Proceedings of the Coastal Structures 2003, Portland, OR, USA, 26–30 August 2003; pp. 369–381. [CrossRef]
35. De Chowdhury, S.; Anand, K.V.; Sannasiraj, S.A.; Sundar, V. Nonlinear wave interaction with curved front sea-walls. *Ocean Eng.* **2017**, *140*, 84–96. [CrossRef]
36. Oh, S.-H.; Jang, S.-C.; Lee, J. *Wave Overtopping and Loading for the Recurved Parapets on the Crest of Rubble Mound Breakwater*; Thomas Telford Ltd.: London, UK, 2018; pp. 979–985. [CrossRef]
37. Trung, L.H.; Linh, D.T.; Tho, T.X.; Duy, N.T.; Tung, T.T. Wave overtopping and splash-up at seawalls with bullnose. *Vietnam. J. Sci. Technol.* **2020**, *20*, 333–342. [CrossRef]
38. Kisacik, D.; Tarakcioglu, G.O.; Cappietti, L. Adaptation measures for seawalls to withstand sea-level rise. *Ocean Eng.* **2022**, *250*, 110958. [CrossRef]
39. Pearson, J.; Bruce, T.; Kortenhaus, A.; van der Meer, J. Effectiveness of recurve walls in reducing wave overtopping on seawalls and breakwaters. *Coast. Eng.* **2004**, *4*, 4404–4416. [CrossRef]
40. Esteban, G.A.; Aristondo, A.; Izquierdo, U.; Blanco, J.M.; Pérez-Moran, G. Experimental analysis and numerical simulation of wave overtopping on a fixed vertical cylinder under regular waves. *Coast. Eng.* **2022**, *173*, 104097. [CrossRef]
41. Franco, L. Vertical breakwaters: The Italian experience. *Coast. Eng.* **1994**, *22*, 31–55. [CrossRef]
42. Allsop, W.; Bruce, T.; Pearson, J.; Besley, P. Wave overtopping at vertical and steep seawalls. *Proc. Inst. Civ. Eng. Marit. Eng.* **2005**, *158*, 103–114. [CrossRef]

43. Hubner, R.G.; Fragassa, C.; Paiva, M.D.S.; Oleinik, P.H.; Gomes, M.D.N.; Rocha, L.A.; Santos, E.D.D.; Machado, B.N.; Isoldi, L.A. Numerical Analysis of an Overtopping Wave Energy Converter Subjected to the Incidence of Irregular and Regular Waves from Realistic Sea States. *J. Mar. Sci. Eng.* **2022**, *10*, 1084. [CrossRef]
44. Galván, J.; Sánchez-Lara, M.J.; Mendikoa, I.; Pérez-Morán, G.; Nava, V.; Rodríguez-Arias, R. NAUTI-LUS-DTU10 MW Floating Offshore Wind Turbine at Gulf of Maine: Public Numerical Models of an Ac-tively Ballasted Semisubmersible. In Proceedings of the WindEurope Conference 2018 within the Global Wind, Hamburg, Germany, 25–28 September 2018; Volume 1102. [CrossRef]
45. Ursell, F. The long-wave paradox in the theory of gravity waves. *Math. Proc. Camb. Philos. Soc.* **1953**, *49*, 685–694. [CrossRef]
46. Chakrabarti, S.K. Offshore Structure Modeling. In *Applied Ocean Research, Advanced Series on Ocean Engineering*; World Scientific Publishing: Singapore, 1994. [CrossRef]
47. Fenton, J.D. A fifth-order Stokes theory for steady waves. *J. Waterw. Port Coast. Ocean Eng.* **1985**, *111*, 216–234. [CrossRef]
48. Windt, C.; Davidson, J.; Schmitt, P.; Ringwood, J. On the assessment of numerical wave makers in CFD simulations. *J. Mar. Sci. Eng.* **2019**, *7*, 47. [CrossRef]